Published in final edited form as:

Magn Reson Med. 2018 February ; 79(2): 1001–1009. doi:10.1002/mrm.27014.

Characterization of tumor vascular permeability using natural dextrans and CEST MRI

Yuguo Li[1,2], **Yuan Qiao**[3], **Hanwei Chen**[2,4], **Renyuan Bai**[5], **Verena Staedtke**[5], **Zheng Han**[1,2], **Jiadi Xu**[1,2], **Kannie W.Y. Chan**[1,2,6], **Nirbhay Yadav**[2], **Jeff W.M. Bulte**[1,2,7], **Shibin Zhou**[3], **Peter C.M. van Zijl**[1,2], and **Guanshu Liu**[1,2,*]

[1]F.M. Kirby Research Center for Functional Brain Imaging, Kennedy Krieger Institute, Baltimore, Maryland [2]Department of Radiology, Johns Hopkins University School of Medicine, Baltimore, Maryland [3]Ludwig Center, Sidney Kimmel Comprehensive Cancer Center, The Johns Hopkins University School of Medicine, Baltimore, Maryland [4]Department of Radiology, Panyu Central Hospital; Guangzhou, China [5]Department of Oncology, Johns Hopkins University School of Medicine, Baltimore, Maryland [6]Department of Mechanical and Biomedical Engineering, City University of Hong Kong, Hong Kong [7]Cellular Imaging Section and Vascular Biology Program, Institute for Cell Engineering, Johns Hopkins University School of Medicine, Baltimore, Maryland

Abstract

Purpose—To investigate the use of natural dextrans as nano-sized Chemical Exchange Saturation Transfer (CEST) MRI probes for characterizing size-dependent tumor vascular permeability.

Methods—Dextrans of different molecular weight (MW) = 10, 70, 150 and 2000 kD were characterized for their CEST contrast. Mice (n=5) bearing CT26 subcutaneous colon tumors were injected i.v. with 10 kD (D10, 6 nm) and 70 kD (D70, 12 nm) dextran at a dose of 375 mg/kg. The CEST MRI signal in the tumors were assessed before and ~40 minutes after each injection using a dynamic CEST imaging scheme.

Results—All dextrans of different MWs have a strong CEST signal with an apparent maximum around 0.9 ppm. The detectability and the effects of pH and saturation conditions (B_1 and T_{sat}) were investigated. When applied to CT26 tumors, the injection of D10 could produce a significant dexCEST enhancement in the majority of the tumor area, while the injection of D70 only resulted in an increase in the tumor periphery. Quantitative analysis revealed the differential permeability of CT26 tumors to different size particles, which was validated by fluorescence imaging and immunohistochemistry.

*Corresponding author: Guanshu Liu, Ph.D., 707 N. Broadway, Baltimore, MD 21205, Phone (office): 443-923-9500; Fax: 410-614-3147, guanshu@mri.jhu.edu.

Competing financial interest statement

J.W.M.B and P.C.M.v.Z are co-founders of and hold an equity ownership in the startup company SenCEST, LLC. Some of the methodologies presented in this paper may ultimately become part of a SenCEST product. This arrangement has been reviewed and approved by the Johns Hopkins University in accordance with its conflict of interest policies.

Conclusions—As a first application, we used 10 kD and 70 kD dextrans to visualize the spatially variable, size-dependent permeability in the tumor, indicating that nano-sized dextrans can be used for characterizing tumor vascular permeability with “dexCEST” MRI and, potentially, for developing dextran-based theranostic drug delivery systems.

Keywords

CEST; MRI; dextran; cancer; permeability

Introduction

Nanomedicine has emerged as a promising means for improving therapeutic indices and reducing the systemic toxicity of traditional chemotherapy. The consequent increase in drug efficacy has led to FDA approval of over 20 nanoparticle therapeutics (1–3). Particles with a molecular weight (MW) larger than 40 kD (the threshold of renal clearance (4)) can, over a period of time, selectively accumulate in the tumor via the enhanced permeability and retention (EPR) effect (4–7). However, there are still several challenges that impede further clinical applications of nanomedicine. One is the highly heterogeneous vascular anatomy in human tumors, resulting in a great spatial variation in particle delivery between different patients or between different parts of the same tumor (8,9). In addition, vessel permeability may differ between different tumor areas. Recent studies have shown that size is the dominant determinant for the pharmacokinetics and biodistribution of nanoparticles (10–16). It is therefore of great interest to develop a non-invasive means to characterize size-dependent vascular permeability and to choose the optimal particle size range for efficient nanoparticle drug delivery. Such a capability may also aid the development of effective vascular targeting therapies, which have been proven to improve the efficacy of (nano)chemotherapy (17). A number of Gd-based macromolecular contrast media (MMCM) (18) with intermediate MW (10–30 kD) and high MW (>30 kD) values have demonstrated improved cancer diagnosis (19) over smaller agents (e.g., Gd-DTPA, MW = 547 D) used in the clinic currently. However, clinical translation of these macromolecular complexes is often impeded by safety concerns related to their slow excretion and possible tissue accumulation, with the potential risk of release of toxic Gd(III) ions (20,21). In the present study, in order to achieve a high clinical translatability, we sought to develop nano-sized dextrans for MR imaging using their hydroxyl groups as a natural ‘magnetic label’ for Chemical Exchange Saturation Transfer (CEST) MRI (22–27).

Several studies by us (28,29) and others (30–36), have shown that the hydroxyl (OH) protons of glucose analogues and glycogen can be imaged via water protons using CEST MRI. Because dextran is composed of multiple glucose units, abundant in hydroxyl (OH) protons (Fig. 1a), native dextran can be detected by CEST MRI directly. This constitutes a natural labeling approach, as no synthetic (radioactive, optical, heteronuclear, or paramagnetic- or super-paramagnetic-based) labels are required, facilitating clinical translation. As a first proof-of-concept study, we demonstrate the use of dextrans of different molecular sizes as nano-sized imaging probes to characterize tumor vascular permeability.

Methods

Chemicals

Unless otherwise noted, dextrans of MW = 10, 70, 150, and 2,000 kD and D-glucose (Sigma) were prepared at a concentration of 3.6 mg/ml (20 mM per glucose unit) in PBS buffer (pH=7.3). Fluorescein-labeled 10 kD and 70 kD dextrans (FITC-dextran) were purchased from Sigma. The mean size (z-average) and size heterogeneity (polydispersity index, PDI) of the purchased dextran particles were measured in PBS at room temperature by dynamic light scattering using a Nanosizer ZS90 (Malvern Instruments, Southborough, MA).

Tumor model

All animal studies were approved by our Institutional Animal Care and Use Committee. Mice bearing subcutaneous murine CT26 colon tumors were prepared as described previously (37,38). In brief, 5×10^5 CT26 cells were injected subcutaneously into the right flank of BALB/c mice (female, six weeks old, Harlan Breeders) and grown for ~14 days. At that time the tumors were approximately 350 mm^3 or larger, with noticeable necrotic cores.

MRI

The *in vitro* CEST contrast of dextran was assessed using a vertical bore Bruker 11.7 T MRI scanner equipped with a 15 mm volume coil (39–41). *In vivo* MR studies were carried out on a Bruker Biospec 11.7 T horizontal MRI scanner equipped with a 23 mm mouse brain volume coil (40,41). Dynamic MR images were acquired according to the diagram shown in Figure 2 to monitor the changes in CEST contrast upon tail vein injection of dextran (375 mg/kg bw). Each CEST scan was acquired using a segmented CEST acquisition scheme of seven pairs of offsets ranging from (±) 0.4 to (±) 1.6 ppm (step=0.2 ppm, ~5 minutes per CEST acquisition). Mice (n=5) were injected i.v. with 300 μL 10 kD dextran in PBS (25 mg/mL, size ~6 nm, 375 mg/kg bw), followed by eight repeated segmented CEST acquisitions. Then, 300 μL 70 kD dextran solution (25 mg/mL, size ~12 nm) was injected at the same dose and another eight CEST acquisitions were acquired. A fat-suppressed RARE sequence with a continuous wave pre-saturation pulse of B_1=1.8 μT and 3 seconds (T_R/T_E=5000/5 ms, RARE factor=10) was used. To correct B_0 inhomogeneity, WASSR-based B_0 maps (42) were acquired before and after CEST acquisition. Contrast-enhanced images were then acquired using a T1w spin echo sequence (TR/TE=18/3 ms) before and 15 minutes after i.v. injection of Gd-DTPA (0.05 mL bolus of 0.5 mmol/mL Magnevist over about 3 s).

Data were processed using custom-written MATLAB scripts. CEST effects are detected by measuring the ratio of the water signal intensity with (S) and without (S_0) saturation as a function of irradiation frequency and quantified by the magnetization transfer ratio asymmetry, $MTR_{asym}=(S^{-\Delta\omega} - S^{+\Delta\omega})/S_0$, where $S^{+\Delta\omega}$ and $S^{-\Delta\omega}$ are the MRI signals with RF irradiation at particular offsets $+\Delta\omega$ and $-\Delta\omega$, respectively, and S_0 is the signal acquired without RF saturation. After correcting for B_0 inhomogeneity using the WASSR method, the *in vivo* CEST contrast was quantified by averaging the $MTR_{asym}=(S^{-\Delta\omega} - S^{+\Delta\omega})/S_0$ from 0.8 to 1.2 ppm (28). To visualize only the enhancement due to the dextran uptake in the tumor, we calculated the ΔMTR_{asym} map at each post-injection time point (t), i.e.

$\Delta MTR_{asym}(t) = MTR_{asym}(t) - MTR_{asym}(t=0)$, with respect to the MTR_{asym} before injection (t=0). This was used for calculating the area under the curve (AUC) pixel-by-pixel over a period of 40 min after the injection of each dextran (43). Intratumoral distributions were quantified using the Enhancing Fraction (f%) — the fraction of the tumor volume with non-zero enhancement (*i.e.,* AUC >0) voxels (43). The DCE-MRI data was processed using a linear algorithm of the reference region model (44) and K^{trans} maps were calculated (Supporting information).

Fluorescence imaging

In vivo and *ex vivo* fluorescence imaging was performed and analyzed with a Spectrum/CT IVIS® *in vivo* imaging system using Living Image® software (PerkinElmer, Waltham, MA). Briefly, mice were injected with a single FITC-dextran (375 mg/kg bw) of either 10 kD (n=3) or 70 kD (n=3) and imaged for one hour. Fluorescence signal (exc/emi = 492/518 nm) was quantified as radiance efficiency.

Immunohistochemistry

Tumors were excised at 30 minutes after a single injection of FITC-10KD dextran (375 mg/kg bw, n=1) or at 1 hour after a single injection FITC-10KD dextran (375 mg/kg bw, n=1) were fixed in PFA and processed for histology. For immunofluorescent staining of CD31 and CD31 rat anti-rabbit mAb (Life Technologies, Inc.) and Alexa Fluor® 594 goat anti-rabbit IgG (H+L chain) antibody (Life Technologies, Inc.) were used as primary and secondary antibodies, respectively. Sections were blocked with 10% goat bovine serum albumin for 30 min, followed by overnight incubation at 4 °C with the primary antibody and 45 min at 4 °C with the secondary antibody. After each step, slides were washed with PBS. Fluorescent images were taken with a Zeiss Axiovert 200 base microscope.

Statistical analysis

Data were expressed as means ± SD and analyzed by unpaired, two-tailed Student's t test assuming equal variances. Differences were considered significant at $P<0.05$.

Results

Characterization of the CEST MRI properties of dextran *in vitro*

The sizes of dextrans are measured using DLS to be 5.9, 12.9, 27.3, and 77.0 nm for MW = 10, 70, 200, and 2000 kD, respectively (Supporting Information, Table S1). Figures 1b–d show that dextrans in the MW range from 10 kD to 2,000 kD have a strong CEST signal with an apparent maximum around 0.9 ppm (B_1=3.6 μT), ranging from 0.196±0.019 to 0.224±0.031 in MTR_{asym}. The CEST signal at 0.9 ppm is similar for the different MW dextrans as compared to that of D-glucose (MTR_{asym} = 0.213±0.016), the monomer composing dextran, with all dissolved at the same glucose unit concentration (Supporting Information, Fig. S1). Higher MW dextrans exhibit a slightly lower CEST contrast than those of smaller size, likely due to the reduced water accessibility of a small portion of hydroxyl protons shielded within larger molecules. However, this effect was not statistically significant. At higher frequency offset (>2 ppm), in contrast, the CEST signals of dextran and glucose are significantly different, attributable to the depletion of α-1C-OH when

glucoses polymerize via α-1,3 linking to form dextran (Fig. 1a). As shown in Figure 1d, the CEST contrast at ~0.9 ppm allows the MRI detection and quantification of dextrans of different MWs.

Similar to D-glucose, the CEST signal of dextrans exhibits a strong pH dependence (Figures 3a&b). At pH=6.5, the CEST contrast (0.385±0.006) was almost three-fold higher than that at pH=7.5 (0.141±0.015), which is advantageous for the detection of dextran in the extravascular extracellular space (EES) of tumors where the pH is often acidic. At physiological pH (~7.3) and an RF irradiation field of 3.6 μT, a detectability of 5% MTR_{asym} (45) of dexCEST MRI is achieved for 3 mM glucose unit concentration (Fig. 1c). This corresponds to concentrations of 54.0, 7.7, 3.6, and 0.3 μM dextran for sizes of 10, 70, 150, and 2,000 kD, respectively. Similar to glucose, dextran also exhibits a highly B_1- and T_{sat}-dependent CEST pattern (Figures. 3c&d). Note that due to the coalescence of OH signal with that of water protons, the maximum of 0.9 ppm is only an apparent one. It becomes visible due to an asymmetry in the water resonance that appears as a peak when performing an asymmetry analysis and removing the direct water saturation contribution that is symmetric. When using higher B_1 or longer T_{sat}, this maximum will shift to higher frequency.

Size-dependent uptake of nano-sized dextrans in tumors

To study the size-dependent dextran uptake in tumors, we designed an imaging scheme as shown in Figure 2. First, a small size dextran was injected and its dexCEST contrast monitored dynamically during a waiting time window (with the length depending on the clearance rate of the dextran injected). Subsequently, a large size dextran was injected and monitored. This design allows the detection of the tumor uptake of two sizes of dextrans in the same tumor within a single MRI session. Such a long scan time under anesthesia could affect for instance tissue hydration and vessel dilation, so the data interpretation has the inherent assumption that tumor physiology remains unchanged. As a simple check for overall physiology, we monitored the respiration rate, which was consistent throughout the experiments. In this first example, we studied the tumor uptake of 10 kD dextran (D10, ~6 nm) and 70 kD dextran (D70, ~13 nm) in CT26 colon tumors. As early as five minutes after the injection of D10 (375 mg/kg body weight), conspicuous dexCEST enhancement appeared, which reached its maximum (average ΔMTR_{asym}=0.017 for the whole tumor) at around 17 minutes post-injection (Fig. 4a). At that time, significant dexCEST enhancement was observed in the majority of the tumor area. However, the washout of D10 was very quick, and most of the dexCEST signal in the tumor disappeared within 33 minutes post-injection. Approximately 40 minutes after the first injection, a time window that allowed the clearance of the majority of D10 from the tumor (46), a second injection was performed with D70. The maximal dexCEST enhancement in the average ΔMTR_{asym} of the whole tumor was only about 0.006, much lower than that induced by D10, as dextrans could not penetrate a large part of the tumor body at this time point. Instead, an increase in dexCEST signal was observed predominantly in the tumor periphery. As expected, the rate of clearance of D70 from the tumor was much slower than that of D10. Fig. 4b also shows the Gd-DTPA contrast enhanced image. Interestingly, the area of uptake appeared smaller, while that of the calculated K^{trans} appears comparable in area to the dextrans.

To study the dynamics of dextran uptake and clearance in different regions, we manually drew two regions of interest (ROI), with ROI 1 showing strong dexCEST signal increase for both D10 and D70, and ROI 2 showing strong CEST signal increase for D10 but not D70 (Fig. 4c). In ROI 1, the injection of D10 led to a maximum ΔMTR_{asym} of 0.064±0.015 at ~22 minutes post-injection, while the injection of D70 resulted in a maximum ΔMTR_{asym} of 0.090±0.013 at ~11 minutes post the injection of D70 (51 minutes post the first injection), indicating that the cut-off value of the vascular pore size must be >12 nm (the diameter of D70) in these regions. As expected, the decay of dexCEST enhancement by D10 was much quicker than that of D70. Conversely, ROI 2 was only permeable to D10, indicating vascular pore sizes smaller than 12 nm, the size of 70 kD dextran, but larger than 6 nm, the size of 10 kD dextran. The maximal D10 dexCEST enhancement in ROI 1 was about three-fold larger than that of ROI 2 (MTR_{asym}=0.064 ±0.015 vs 0.021±0.014), indicating a higher permeability. To assess the differential permeability to different size particles of the same tumor, we calculated the AUC (Fig. 5a) and enhancing fraction (f%, Fig. 5b) of 10 kD and 70 kD dextrans in each tumor (n=5). The results showed significant differences between the 10 and 70 kD dextrans (i.e., $P<0.05$ for both AUC and f%), indicative of size-dependent vascular permeability.

We also conducted *in vivo* fluorescence imaging to validate the MRI findings, which is feasible for superficial subcutaneous tumors when fluorescence-tagged dextrans are used (i.e., FITC-dextran). The fluorescence imaging results (Fig. 6) confirm the MRI data in that the fluorescence intensity in D10-injected mice disappeared faster than that in D70 mice. We further confirmed extravasation of the dextrans by performing immunohistochemistry of the tumors. i.e., dextran (green, FITC-tagged) and blood vessels (red, CD31 staining) as shown in Figure 7. Interestingly, a difference in the spatial distribution of dextran molecules was found between D10 and D70 (Fig. 7, and Supporting information Figure S2), indicating a different penetration depth for dextrans of different sizes after extravasation.

Discussion

Dextran is a family of natural polysaccharides that has been used widely in clinical and in pre-clinical studies, with a well-characterized safety profile. Medical dextran is available in a range of molecular sizes, i.e., from 5.9 to 77.0 nm. The availability of a broad size range, together with being neutrally charged, makes dextran an ideal marker for assessing the size-dependent permeability of membranes and biological compartments. Fluorescence-labeled dextran (MW=2.3 kD) has a long history of measuring tissue permeability since the 1970s (47), for example, to assess blood-brain barrier permeability (48,49) and solid tumor permeability (50). For MRI, dextran has been considered a versatile polymer platform to create paramagnetic macromolecular MRI contrast agents (51,52). However, none of these metallic agents have yet gained clinical acceptance primarily due to the possible toxicity related to their prolonged retention time in the body and the risk of free metal release (53). The use of inherent CEST contrast carried naturally by dextran molecules eliminates the requirement of chemical labels. Our study clearly shows that our dexCEST approach is an effective imaging tool, allowing the study of delivery kinetics and spatial distribution of dextrans of different sizes in tumors.

It is known that the rate for molecules to extravasate into the interstitial space is highly dependent on their size and shape, with a nonlinear relationship (21,54). Because of that, traditional small molecule-based (e.g., Gd-DTPA, MW=547) dynamic contrast-enhanced (DCE) MRI is unable to accurately predict permeability in the macro- and nano- size range, a size range more suitable for the characterization of microvessels (55). Actually, our results are interesting in that respect. While the K^{trans} map appears very similar to the dextran enhancement, the pattern in the static Gd-CE enhancement appears to indicate a smaller area than the dextran. This seems unexpected as the Gd molecular weight (547D, < 1 nm (56)) is much smaller than that of the dextrans. This confirms expectations of Gd-DTPA not being reflective of nanoparticle properties. We suggest that it is difficult to directly compare Gd-enhancement and dexCEST-enhancement quantitatively for three reasons: 1) the doses of dextrans are much larger than that of the Gd-DTPA; 2) the shape and surface properties of dextrans and Gd-DTPA are different; and 3) the time points of imaging are different. It is well known that larger molecules have a slower pharmacokinetics than smaller ones, hence the dextrans are cleared from tissues at a slower rate. This may be one explanation why Gd-DTPA shows relatively smaller enhancement (at 15 minutes) than dextrans.

Moreover, the clinical translation of Gd-based macromolecular complexes is limited by safety concerns. Our approach employs native dextrans that are commercially available over a size range from intermediate to high MW (up to 2 MD dextran). This offers a simple but effective means by which to assess tissue permeability to nanometer particles of different sizes ranging from a few nm to about 77 nm (50). Our findings are consistent with previous studies obtained using intravital imaging of FITC-dextran of different sizes (57). We expect that size-dependent tumor uptake of dextran can provide useful insight into the characteristics of the targeted tumors, which is ultimately important for designing the appropriate nanoparticle chemotherapy. It should be noted that our current approach focuses on the tumor uptake of dextran in the very early phase (i.e., <1 hour), which mainly reflects the cut-off range of the tumor vessel pore size (58). It should also be noted that both vascular permeability and tissue penetration can contribute to the intratumoral accumulation of an agent, which can't be completely separated in our CEST MRI results. However, as reported previously by Dreher et al using intravital microscope (46), the tumor penetration distances were estimated to be ~35 μm and ~15 μm for 10 kD and 70 kD dextrans respectively. Considering the spatial resolution of our CEST MRI was ~ 200 μm, we conclude that vascular permeability most likely is the predominant contributor to the dexCEST contrast enhancement. It should also be noted that the cut-off used in this work is not a single threshold of the physical size permeable to the tumor, but a reflection of distributions of dextran sizes and tumor permeabilities (12). It should also be noted that the validation using *in vivo* fluorescence imaging is not quantitative because it was performed separately on different animals, not sequentially on the same animal as dexCEST MRI. The reason was that both 10kD and 70 kD dextrans were labeled with FITC, making the differentiation of tumor uptake of different dextrans difficult. Also, because FITC emits green light (exc/emi = 492/518 nm), quantitation of *in vivo* fluorescence in different parts of the tumor is also difficult. Comprehensive quantitative *in vivo* fluorescence imaging validation requires synthesized dextrans with different NIR dyes, which will be pursued in our future studies. One potentially confounding effect for time dependent CEST studies is a change in B_0

homogeneity during the study. To monitor for this, we acquired WASSR field maps during these studies (See Supporting information Figure S3), which showed insufficient changes to affect the quantification of the results.

The use of simple dextrans as imaging agents is expected to provide a great advantage over labeled dextrans, in that native dextran has been widely used in the clinic as an injectable agent for more than five decades, with a proven safety profile even at very high doses (59). The dose used in this study (375 mg/kg) falls well within the clinical dose of 70 KD dextran as plasma expander (1.5 g/kg) (60). While dextrans, like other intravenously administered colloids, may induce anaphylactoid/ic reactions (61,62), the possibility of severe dextran-induced allergic reactions can be reduced substantially by pretreating with small size dextran 1 (1 kD), making dextran at least as safe as albumin and starches (63,64). This is expected to greatly accelerate translation of the proposed technology to the clinic. Although we demonstrated our technique using an 11.7T high-field small-animal MRI scanner, it has been shown that CEST technologies can be quickly translated from pre-clinical scanners (e.g., 4.7, 9.4, or 11.7T) to clinical scanners (i.e., 3T) (29,65,66), and from rodent models to patients (66,67). Hence, the clinical translation of dexCEST MRI, after being fully validated in preclinical studies, can be relatively fast.

Conclusion

In summary, we characterized the CEST properties of natural dextran of different sizes and developed a new natural labeling MRI approach in which nano-sized dextrans can be used as MRI contrast agents. We then demonstrated the usefulness of these dextrans in characterizing the size-dependent vascular permeability of solid tumors. Our results reveal that dexCEST can be used to monitor the dynamics as well as the spatial distribution of the changes in tumor vascular permeability.

Supplementary Material

Refer to Web version on PubMed Central for supplementary material.

Acknowledgments

This work was supported by NIH grants R03 EB021573, R01 CA211087, R21 CA215860, RO1 EB019934, R01 EB015032, R01 EB012590, P50 CA062924 and The Virginia and D.K. Ludwig Fund for Cancer Research.

References

1. Davis ME, Chen ZG, Shin DM. Nanoparticle therapeutics: an emerging treatment modality for cancer. Nature reviews Drug discovery. 2008; 7(9):771–782. [PubMed: 18758474]
2. Jain RK, Stylianopoulos T. Delivering nanomedicine to solid tumors. Nature reviews Clinical oncology. 2010; 7(11):653–664.
3. Zhang L, Gu FX, Chan JM, Wang AZ, Langer RS, Farokhzad OC. Nanoparticles in medicine: therapeutic applications and developments. Clinical pharmacology and therapeutics. 2008; 83(5): 761–769. [PubMed: 17957183]
4. Maeda H, Wu J, Sawa T, Matsumura Y, Hori K. Tumor vascular permeability and the EPR effect in macromolecular therapeutics: a review. J Control Release. 2000; 65(1–2):271–284. [PubMed: 10699287]

5. Matsumura Y, Maeda H. A new concept for macromolecular therapeutics in cancer chemotherapy: mechanism of tumoritropic accumulation of proteins and the antitumor agent smancs. Cancer Res. 1986; 46(12 Pt 1):6387–6392. [PubMed: 2946403]
6. Maeda H. The enhanced permeability and retention (EPR) effect in tumor vasculature: the key role of tumor-selective macromolecular drug targeting. Adv Enzyme Regul. 2001; 41(1):189–207. [PubMed: 11384745]
7. Maeda H. Tumor-selective delivery of macromolecular drugs via the EPR effect: background and future prospects. Bioconjug Chem. 2010; 21(5):797–802. [PubMed: 20397686]
8. Tredan O, Galmarini CM, Patel K, Tannock IF. Drug resistance and the solid tumor microenvironment. J Natl Cancer Inst. 2007; 99(19):1441–1454. [PubMed: 17895480]
9. Olive KP, Jacobetz MA, Davidson CJ, Gopinathan A, McIntyre D, Honess D, Madhu B, Goldgraben MA, Caldwell ME, Allard D, Frese KK, Denicola G, Feig C, Combs C, Winter SP, Ireland-Zecchini H, Reichelt S, Howat WJ, Chang A, Dhara M, Wang L, Ruckert F, Grutzmann R, Pilarsky C, Izeradjene K, Hingorani SR, Huang P, Davies SE, Plunkett W, Egorin M, Hruban RH, Whitebread N, McGovern K, Adams J, Iacobuzio-Donahue C, Griffiths J, Tuveson DA. Inhibition of Hedgehog signaling enhances delivery of chemotherapy in a mouse model of pancreatic cancer. Science. 2009; 324(5933):1457–1461. [PubMed: 19460966]
10. Anderson CJ, Ferdani R. Copper-64 radiopharmaceuticals for PET imaging of cancer: advances in preclinical and clinical research. Cancer Biother Radiopharm. 2009; 24(4):379–393. [PubMed: 19694573]
11. Harrington KJ, Mohammadtaghi S, Uster PS, Glass D, Peters AM, Vile RG, Stewart JS. Effective targeting of solid tumors in patients with locally advanced cancers by radiolabeled pegylated liposomes. Clinical cancer research : an official journal of the American Association for Cancer Research. 2001; 7(2):243–254. [PubMed: 11234875]
12. Yuan F, Dellian M, Fukumura D, Leunig M, Berk DA, Torchilin VP, Jain RK. Vascular permeability in a human tumor xenograft: molecular size dependence and cutoff size. Cancer Res. 1995; 55(17):3752–3756. [PubMed: 7641188]
13. Toy R, Hayden E, Camann A, Berman Z, Vicente P, Tran E, Meyers J, Pansky J, Peiris PM, Wu H, Exner A, Wilson D, Ghaghada KB, Karathanasis E. Multimodal in vivo imaging exposes the voyage of nanoparticles in tumor microcirculation. ACS nano. 2013; 7(4):3118–3129. [PubMed: 23464827]
14. Popovic Z, Liu W, Chauhan VP, Lee J, Wong C, Greytak AB, Insin N, Nocera DG, Fukumura D, Jain RK, Bawendi MG. A nanoparticle size series for in vivo fluorescence imaging. Angewandte Chemie. 2010; 49(46):8649–8652. [PubMed: 20886481]
15. De Jong WH, Hagens WI, Krystek P, Burger MC, Sips AJ, Geertsma RE. Particle size-dependent organ distribution of gold nanoparticles after intravenous administration. Biomaterials. 2008; 29(12):1912–1919. [PubMed: 18242692]
16. Jun, Y-w, Huh, Y-M., Choi, J-s, Lee, J-H., Song, H-T., Kim, S., Kim, S., Yoon, S., Kim, K-S., Shin, J-S. Nanoscale size effect of magnetic nanocrystals and their utilization for cancer diagnosis via magnetic resonance imaging. Journal of the American Chemical Society. 2005; 127(16):5732–5733. [PubMed: 15839639]
17. Chauhan VP, Stylianopoulos T, Martin JD, Popovic Z, Chen O, Kamoun WS, Bawendi MG, Fukumura D, Jain RK. Normalization of tumour blood vessels improves the delivery of nanomedicines in a size-dependent manner. Nature nanotechnology. 2012; 7(6):383–388.
18. Brasch R, Turetschek K. MRI characterization of tumors and grading angiogenesis using macromolecular contrast media: status report. European journal of radiology. 2000; 34(3):148–155. [PubMed: 10927157]
19. Su MY, Wang Z, Carpenter PM, Lao X, Mühler A, Nalcioglu O. Characterization of N-ethyl-N-nitrosourea-induced malignant and benign breast tumors in rats by using three MR contrast agents. Journal of Magnetic Resonance Imaging. 1999; 9(2):177–186. [PubMed: 10077011]
20. Schmiedl U, Ogan M, Paajanen H, Marotti M, Crooks LE, Brito AC, Brasch RC. Albumin Labeled with Gd-Dtpa as an Intravascular, Blood Pool Enhancing Agent for Mr Imaging - Biodistribution and Imaging Studies. Radiology. 1987; 162(1):205–210. [PubMed: 3786763]

21. Wu X, Feng Y, Jeong EK, Emerson L, Lu ZR. Tumor characterization with dynamic contrast enhanced magnetic resonance imaging and biodegradable macromolecular contrast agents in mice. Pharmaceutical research. 2009; 26(9):2202–2208. [PubMed: 19597972]
22. van Zijl P, Sehgal AA. Proton Chemical Exchange Saturation Transfer (CEST) MRS and MRI. eMagRes. 2016; 5:1–26.
23. van Zijl PCM, Lam WW, Xu J, Knutsson L, Stanisz GJ. Magnetization Transfer Contrast and Chemical Exchange Saturation Transfer MRI. Features and analysis of the field-dependent saturation spectrum. Neuroimage. 2017; doi: 10.1016/j.neuroimage.2017.04.045
24. Jones KM, Pollard AC, Pagel MD. Clinical applications of chemical exchange saturation transfer (CEST) MRI. J Magn Reson Imaging. 2017; doi: 10.1002/jmri.25838
25. McMahon MT, Chan K. Developing MR probes for molecular imaging. Advances in cancer research. 2013; 124:297–327.
26. Liu G, Song X, Chan KW, McMahon MT. Nuts and bolts of chemical exchange saturation transfer MRI. NMR Biomed. 2013; 26(7):810–828. [PubMed: 23303716]
27. van Zijl P, Yadav NN. Chemical exchange saturation transfer (CEST): what is in a name and what isn't? Magnetic resonance in medicine. 2011; 65(4):927–948. [PubMed: 21337419]
28. Chan KW, McMahon MT, Kato Y, Liu G, Bulte JW, Bhujwalla ZM, Artemov D, van Zijl PC. Natural D-glucose as a biodegradable MRI contrast agent for detecting cancer. Magnetic resonance in medicine : official journal of the Society of Magnetic Resonance in Medicine / Society of Magnetic Resonance in Medicine. 2012; 68(6):1764–1773.
29. van Zijl PC, Jones CK, Ren J, Malloy CR, Sherry AD. MRI detection of glycogen in vivo by using chemical exchange saturation transfer imaging (glycoCEST). Proc Natl Acad Sci U S A. 2007; 104(11):4359–4364. [PubMed: 17360529]
30. Jin T, Mehrens H, Hendrich KS, Kim SG. Mapping brain glucose uptake with chemical exchange-sensitive spin-lock magnetic resonance imaging. Journal of cerebral blood flow and metabolism : official journal of the International Society of Cerebral Blood Flow and Metabolism. 2014; 34(8): 1402–1410.
31. Walker-Samuel S, Ramasawmy R, Torrealdea F, Rega M, Rajkumar V, Johnson SP, Richardson S, Goncalves M, Parkes HG, Arstad E, Thomas DL, Pedley RB, Lythgoe MF, Golay X. In vivo imaging of glucose uptake and metabolism in tumors. Nature medicine. 2013; 19(8):1067–1072.
32. Rivlin M, Tsarfaty I, Navon G. Functional molecular imaging of tumors by chemical exchange saturation transfer MRI of 3-O-Methyl-D-glucose. Magnetic resonance in medicine : official journal of the Society of Magnetic Resonance in Medicine / Society of Magnetic Resonance in Medicine. 2014; 72(5):1375–1380.
33. Rivlin M, Navon G. CEST MRI of 3-O-methyl-D-glucose on different breast cancer models. Magnetic resonance in medicine : official journal of the Society of Magnetic Resonance in Medicine / Society of Magnetic Resonance in Medicine. 2017; doi: 10.1002/mrm.26752
34. Rivlin M, Navon G. Glucosamine and N-acetyl glucosamine as new CEST MRI agents for molecular imaging of tumors. Scientific reports. 2016; 6
35. Cobb JG, Li K, Xie J, Gochberg DF, Gore JC. Exchange-mediated contrast in CEST and spin-lock imaging. Magn Reson Imaging. 2014; 32(1):28–40. [PubMed: 24239335]
36. Ward KM, Aletras AH, Balaban RS. A new class of contrast agents for MRI based on proton chemical exchange dependent saturation transfer (CEST). J Magn Reson. 2000; 143(1):79–87. [PubMed: 10698648]
37. Agrawal N, Bettegowda C, Cheong I, Geschwind JF, Drake CG, Hipkiss EL, Tatsumi M, Dang LH, Diaz LA, Pomper M. Bacteriolytic therapy can generate a potent immune response against experimental tumors. Proceedings of the National Academy of Sciences of the United States of America. 2004; 101(42):15172. [PubMed: 15471990]
38. Qiao Y, Huang X, Nimmagadda S, Bai R, Staedtke V, Foss CA, Cheong I, Holdhoff M, Kato Y, Pomper MG, Riggins GJ, Kinzler KW, Diaz LA Jr, Vogelstein B, Zhou S. A robust approach to enhance tumor-selective accumulation of nanoparticles. Oncotarget. 2011; 2(1–2):59–68. [PubMed: 21378416]

39. Liu G, Gilad AA, Bulte JW, van Zijl PC, McMahon MT. High-throughput screening of chemical exchange saturation transfer MR contrast agents. Contrast media & molecular imaging. 2010; 5(3): 162–170. [PubMed: 20586030]
40. Liu H, Jablonska A, Li Y, Cao S, Liu D, Chen H, Van Zijl PC, Bulte JW, Janowski M, Walczak P, Liu G. Label-free CEST MRI Detection of Citicoline-Liposome Drug Delivery in Ischemic Stroke. Theranostics. 2016; 6(10):1588–1600. [PubMed: 27446492]
41. Li Y, Chen H, Xu J, Yadav NN, Chan KW, Luo L, McMahon MT, Vogelstein B, van Zijl PC, Zhou S, Liu G. CEST theranostics: label-free MR imaging of anticancer drugs. Oncotarget. 2016; 7(6): 6369–6378. [PubMed: 26837220]
42. Kim M, Gillen J, Landman BA, Zhou J, van Zijl PC. Water saturation shift referencing (WASSR) for chemical exchange saturation transfer (CEST) experiments. Magnetic resonance in medicine : official journal of the Society of Magnetic Resonance in Medicine / Society of Magnetic Resonance in Medicine. 2009; 61(6):1441–1450.
43. Alic L, van Vliet M, van Dijke CF, Eggermont AM, Veenland JF, Niessen WJ. Heterogeneity in DCE-MRI parametric maps: a biomarker for treatment response? Physics in medicine and biology. 2011; 56(6):1601–1616. [PubMed: 21335648]
44. Cardenas-Rodriguez J, Howison CM, Pagel MD. A linear algorithm of the reference region model for DCE-MRI is robust and relaxes requirements for temporal resolution. Magn Reson Imaging. 2013; 31(4):497–507. [PubMed: 23228309]
45. Aime S, Delli Castelli D, Terreno E. Highly Sensitive MRI Chemical Exchange Saturation Transfer Agents Using Liposomes. Angewandte Chemie. 2005; 117(34):5649–5651.
46. Dreher MR, Liu W, Michelich CR, Dewhirst MW, Yuan F, Chilkoti A. Tumor vascular permeability, accumulation, and penetration of macromolecular drug carriers. J Natl Cancer Inst. 2006; 98(5):335–344. [PubMed: 16507830]
47. Rutili G, Arfors KE. Fluorescein-labelled dextran measurement in interstitial fluid in studies of macromolecular permeability. Microvascular research. 1976; 12(2):221–230. [PubMed: 979669]
48. Ziylan YZ, Robinson PJ, Rapoport SI. Blood-brain barrier permeability to sucrose and dextran after osmotic opening. Am J Physiol. 1984; 247(4 Pt 2):R634–638. [PubMed: 6208789]
49. Armstrong BK, Robinson PJ, Rapoport SI. Size-dependent blood-brain barrier opening demonstrated with [14C]sucrose and a 200,000-Da [3H]dextran. Experimental neurology. 1987; 97(3):686–696. [PubMed: 2442027]
50. Dreher MR, Liu W, Michelich CR, Dewhirst MW, Yuan F, Chilkoti A. Tumor vascular permeability, accumulation, and penetration of macromolecular drug carriers. J Natl Cancer Inst. 2006; 98(5):335–344. [PubMed: 16507830]
51. Gibby WA, Bogdan A, Ovitt TW. Cross-linked DTPA polysaccharides for magnetic resonance imaging. Synthesis and relaxation properties. Invest Radiol. 1989; 24(4):302–309. [PubMed: 2745011]
52. Wang SC, Wikstrom MG, White DL, Klaveness J, Holtz E, Rongved P, Moseley ME, Brasch RC. Evaluation of Gd-DTPA-labeled dextran as an intravascular MR contrast agent: imaging characteristics in normal rat tissues. Radiology. 1990; 175(2):483–488. [PubMed: 1691513]
53. Cipolla L, Gregori M, So PW. Glycans in magnetic resonance imaging: determinants of relaxivity to smart agents, and potential applications in biomedicine. Current medicinal chemistry. 2011; 18(7):1002–1018. [PubMed: 21254975]
54. Langereis S, De Lussanet QG, Van Genderen MH, Backes WH, Meijer E. Multivalent contrast agents based on gadolinium-diethylenetriaminepentaacetic acid-terminated poly (propylene imine) dendrimers for magnetic resonance imaging. Macromolecules. 2004; 37(9):3084–3091.
55. Kaiser WA, Reiser M. False-Positive Cases in Dynamic Mr Mammography. Radiology. 1992; 185:245–245.
56. Su MY, Muhler A, Lao XY, Nalcioglu O. Tumor characterization with dynamic contrast-enhanced MRI using MR contrast agents of various molecular weights. Magnetic Resonance in Medicine. 1998; 39(2):259–269. [PubMed: 9469709]
57. Dvorak HF, Nagy JA, Dvorak JT, Dvorak AM. Identification and characterization of the blood vessels of solid tumors that are leaky to circulating macromolecules. The American journal of pathology. 1988; 133(1):95–109. [PubMed: 2459969]

58. Gerlowski LE, Jain RK. Microvascular permeability of normal and neoplastic tissues. Microvascular research. 1986; 31(3):288–305. [PubMed: 2423854]

59. Dubick MA, Wade CE. A review of the efficacy and safety of 7.5% NaCl/6% dextran 70 in experimental animals and in humans. J Trauma. 1994; 36(3):323–330. [PubMed: 7511708]

60. McCahon R, Hardman J. Pharmacology of plasma expanders. Anaesthesia & Intensive Care Medicine. 2007; 8(2):79–81.

61. Hedin H, Richter W. Pathomechanisms of dextran-induced anaphylactoid/anaphylactic reactions in man. Int Arch Allergy Appl Immunol. 1982; 68(2):122–126. [PubMed: 6176555]

62. Kraft D, Hedin H, Richter W, Scheiner O, Rumpold H, Devey ME. Immunoglobulin class and subclass distribution of dextran-reactive antibodies in human reactors and non reactors to clinical dextran. Allergy. 1982; 37(7):481–489. [PubMed: 6185010]

63. Ljungström K-G. Dextran 40 therapy made safer by pretreatment with dextran 1. Plastic and reconstructive surgery. 2007; 120(1):337–340. [PubMed: 17572583]

64. Zinderman CE, Landow L, Wise RP. Anaphylactoid reactions to Dextran 40 and 70: reports to the United States Food and Drug Administration, 1969 to 2004. Journal of vascular surgery. 2006; 43(5):1004–1009. [PubMed: 16678697]

65. Jones CK, Schlosser MJ, van Zijl PC, Pomper MG, Golay X, Zhou J. Amide proton transfer imaging of human brain tumors at 3T. Magnetic resonance in medicine : official journal of the Society of Magnetic Resonance in Medicine / Society of Magnetic Resonance in Medicine. 2006; 56(3):585–592.

66. Zhu H, Jones CK, van Zijl PC, Barker PB, Zhou J. Fast 3D chemical exchange saturation transfer (CEST) imaging of the human brain. Magnetic resonance in medicine : official journal of the Society of Magnetic Resonance in Medicine / Society of Magnetic Resonance in Medicine. 2010; 64(3):638–644.

67. Wen Z, Hu S, Huang F, Wang X, Guo L, Quan X, Wang S, Zhou J. MR imaging of high-grade brain tumors using endogenous protein and peptide-based contrast. NeuroImage. 2010; 51(2):616–622. [PubMed: 20188197]

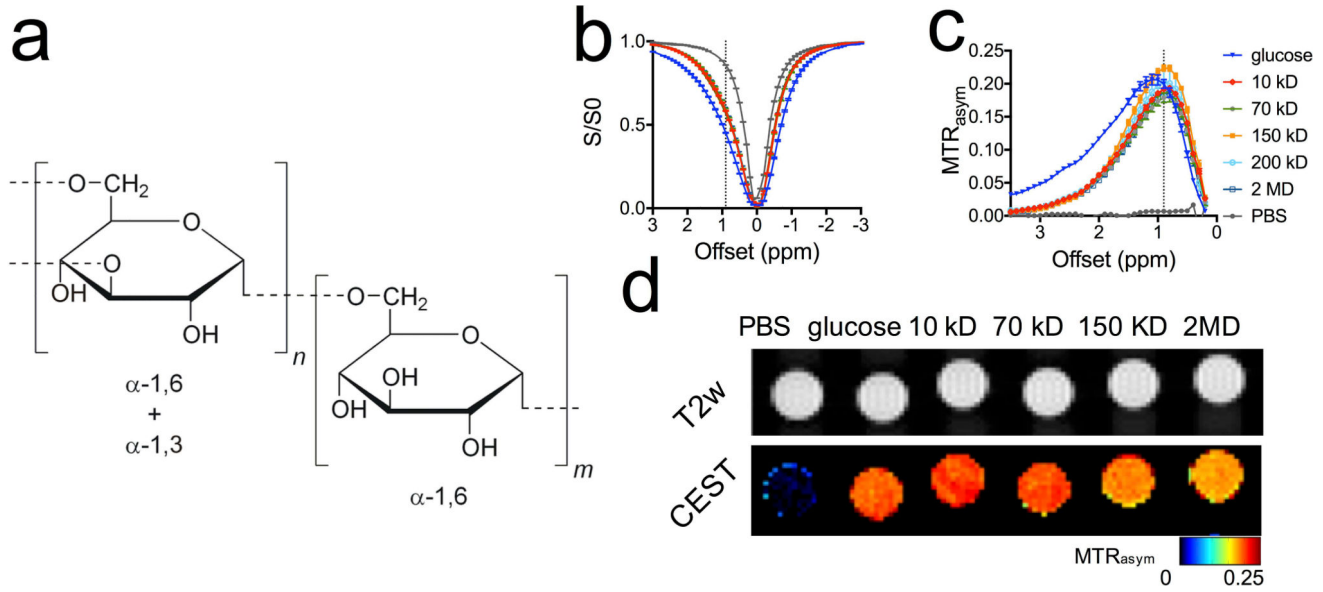

Figure 1. CEST MRI detection of dextrans

a) Chemical structure of dextran. **b)** Z spectra. **c)** MTR_{asym} plots. **d**) CEST parametric maps (quantified by MTR_{asym} at 0.9 ppm) of PBS, 20 mM glucose, and dextrans of 10, 70, 150, and 2,000 KD (20 mM on a glucose unit basis). All samples were prepared at pH=7.3 in 10 mM PBS, and the CEST MRI was acquired using a 4-second long CW RF pulse (B_1=3.6 μT) at 37 °C.

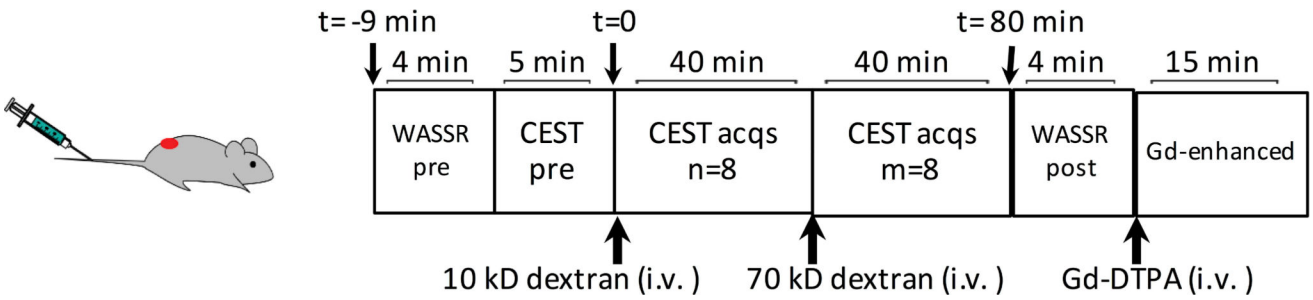

Figure 2. Illustration diagram of the dynamic imaging protocol

dexCEST signals were acquired sequentially after the injection of 10 kD dextran (~6 nm, 375 mg/kg bw) and after the injection of 70 kD dextran (~12 nm, 375 mg/kg bw), followed by the contrast-enhanced MRI (Gd-DTPA, 0.5 mmol/kg bw).

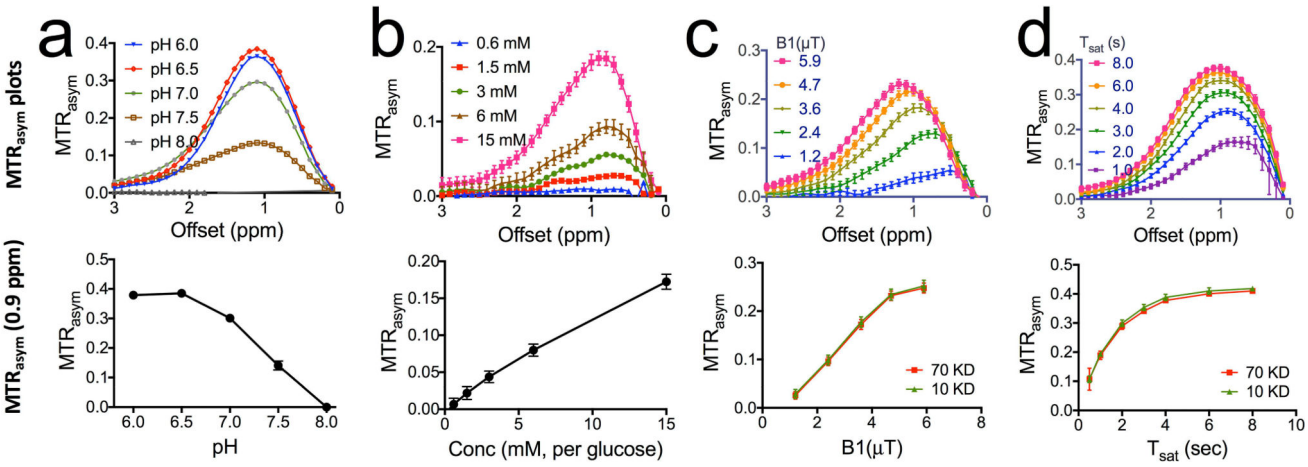

Figure 3. Characterization of CEST MRI signal for 70 kD dextran

a) MTR_{asym} plots of 20 mM D70 at different pH (top) and pH-dependence of dexCEST contrast quantified by MTR_{asym} at 0.9 ppm (bottom). **b)** MTR_{asym} plots of D70 at different concentrations (top) and **c**oncentration-dependence of dexCEST contrast quantified by MTR_{asym} at 0.9 ppm (bottom). **c)** MTR_{asym} plots of 20 mM D70 acquired using different B_1 (top) and the B_1-dependence of dexCEST contrast of both D10 and D70 as quantified by MTR_{asym} at 0.9 ppm. **d)** MTR_{asym} plots of 20 mM D70 acquired using different T_{sat} (top) and the T_{sat}- dependence of dexCEST contrast of both D10 and D70 as quantified by MTR_{asym} at 0.9 ppm (bottom). Unless otherwise stated, all samples were prepared in 10 mM PBS pH=7.3, and the CEST MRI was acquired using a 4-second long CW RF pulse (B_1=3.6 μT) at 37 °C.

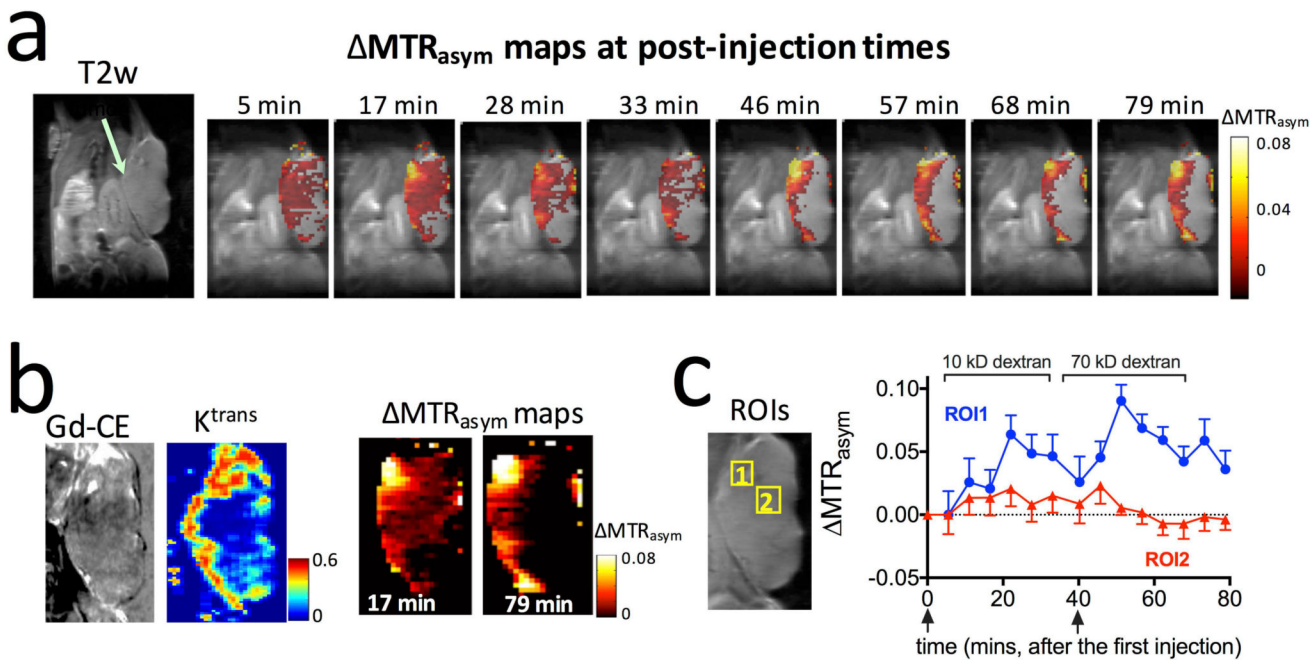

Figure 4. Size-dependent tumor uptake of 10 and 70 kD dextrans detected by CEST MRI

a) Anatomical T2w images and dynamic dexCEST MRI showing distinctive tumor uptake of 10 kD and 70 kD dextran in terms of spatial distribution and pharmacokinetics. **b**) Zoomed view of the Gd contrast-enhanced image, permeability (K^{trans}) map, and corresponding ΔMTR_{asym} maps at 17 and 79 minutes, respectively. **c**) Dynamic change of the dexCEST signal in the two ROIs (marked in zoomed view of T2w image on the left).

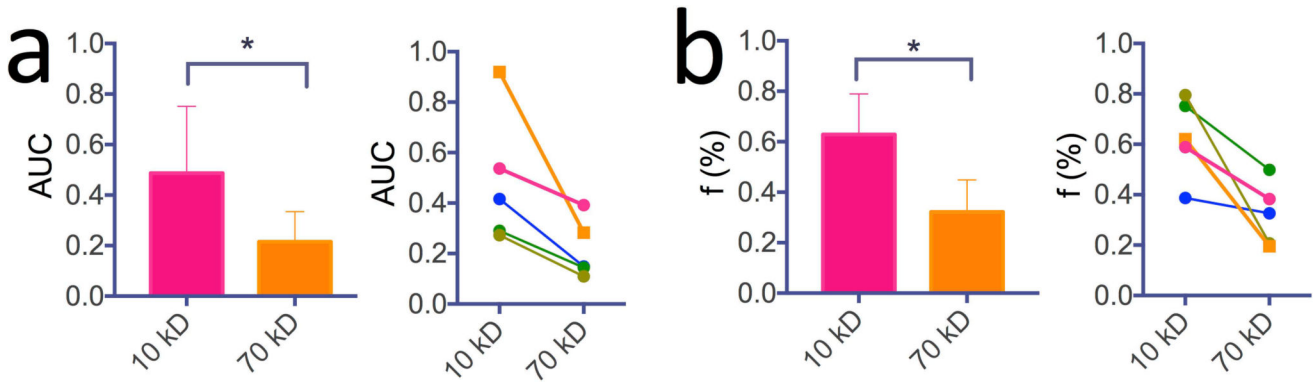

Figure 5. Quantitative comparison of the size-dependent tumor uptake of 10 and 70 kD dextrans detected by CEST MRI in five animals

a) Bar plot of mean values (left) and comparison in each tumor (right) of the area under curve (AUC) after the injection of 10kD and 70 kD dextrans ($P<0.05$, n=5). **b**) Bar plot of mean values (left) and comparison in each tumor (right) of the enhancing fraction (f%) after the injection of 10 kD and 70 kD dextrans ($P<0.05$, n=5).

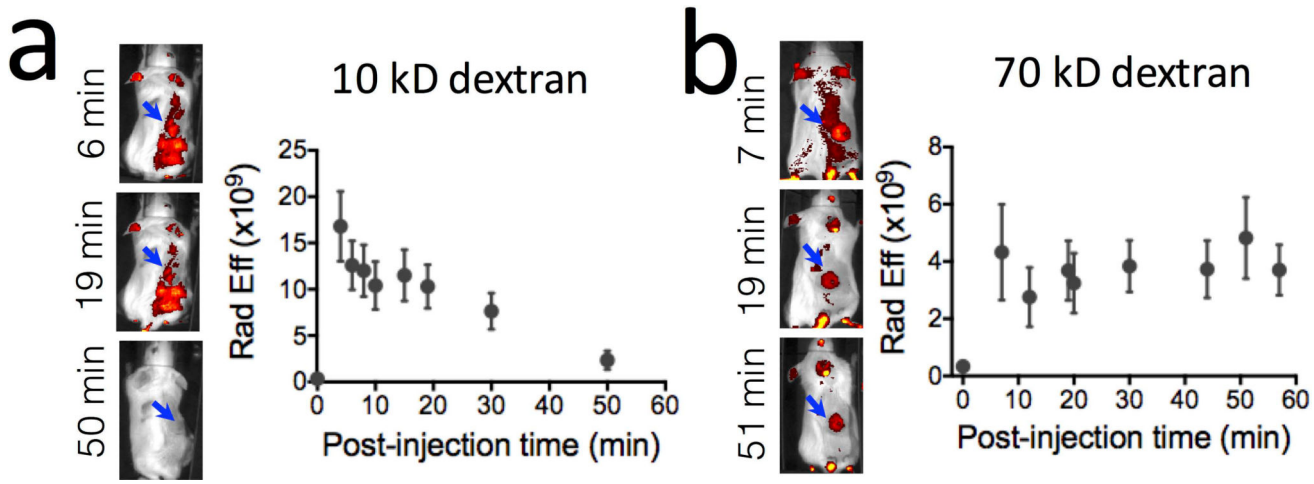

Figure 6. ***In vivo*** **Fluorescence imaging**

Fluorescence images of FITC-dextran of 10 kD (**a**) and 70 kD (**b**) and the corresponding dynamic change in the average fluorescence intensity in the tumor region after the injection of FITC-dextran.

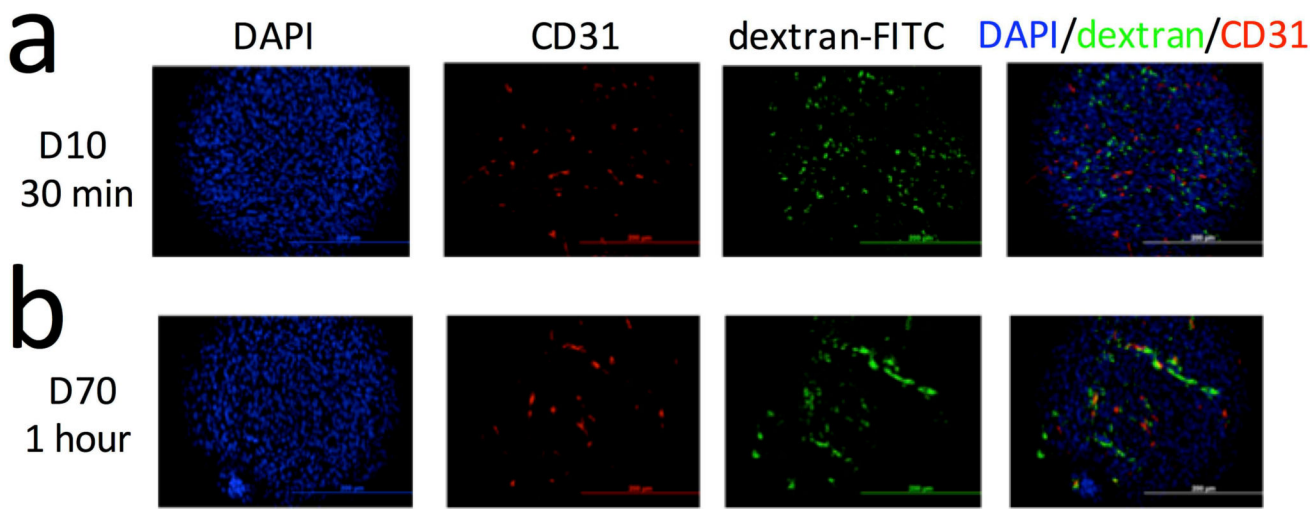

Figure 7. Immunohistochemical validation

Immunohistochemistry of the tumor (DAPI=tumor cells (blue), CD31=endothelial cells (red), and FITC-dextran (green)) at 30 minutes after the injection of D10 (**a**) or 1 hour after the injection of D70 (**b**). The overlaid images of DAPI, CD31, and dextran-FITC show the extravasation of dextran of both MWs. Scale bar=200 μm.